OPTICA

Modular chip-integrated photonic control of artificial atoms in diamond waveguides

Kevin J. Palm,[1,*,†] Mark Dong,[1,2,7,†] D. Andrew Golter,[1] Genevieve Clark,[1,2] Matthew Zimmermann,[1] Kevin C. Chen,[2] Linsen Li,[2] Adrian Menssen,[2] Andrew J. Leenheer,[3] Daniel Dominguez,[3] Gerald Gilbert,[4,8] Matt Eichenfield,[3,5,9] and Dirk Englund[2,6,10]

[1]The MITRE Corporation, 202 Burlington Road, Bedford, Massachusetts 01730, USA
[2]Research Laboratory of Electronics, Massachusetts Institute of Technology, Cambridge, Massachusetts 02139, USA
[3]Sandia National Laboratories, P.O. Box 5800, Albuquerque, New Mexico 87185, USA
[4]The MITRE Corporation, 200 Forrestal Road, Princeton, New Jersey 08540, USA
[5]College of Optical Sciences, University of Arizona, Tucson, Arizona 85719, USA
[6]Brookhaven National Laboratory, 98 Rochester St, Upton, New York 11973, USA
[7]mdong@mitre.org
[8]ggilbert@mitre.org
[9]eichenfield@arizona.edu
[10]englund@mit.edu
[†]These authors contributed equally to this work.
*kpalm@mitre.org

Received 23 January 2023; revised 24 March 2023; accepted 15 April 2023; published 18 May 2023

A central goal in creating long-distance quantum networks and distributed quantum computing is the development of interconnected and individually controlled qubit nodes. Atom-like emitters in diamond have emerged as a leading system for optically networked quantum memories, motivating the development of visible-spectrum, multi-channel photonic integrated circuit (PIC) systems for scalable atom control. However, it has remained an open challenge to realize optical programmability with a qubit layer that can achieve high optical detection probability over many optical channels. Here, we address this problem by introducing a modular architecture of piezoelectrically actuated atom-control PICs (APICs) and artificial atoms embedded in diamond nanostructures designed for high-efficiency free-space collection. The high-speed four-channel APIC is based on a splitting tree mesh with triple-phase shifter Mach–Zehnder interferometers. This design simultaneously achieves optically broadband operation at visible wavelengths, high-fidelity switching (>40 dB) at low voltages, submicrosecond modulation timescales (>30 MHz), and minimal channel-to-channel crosstalk for repeatable optical pulse carving. Via a reconfigurable free-space interconnect, we use the APIC to address single silicon vacancy color centers in individual diamond waveguides with inverse tapered couplers, achieving efficient single photon detection probabilities (∼15%) and second-order autocorrelation measurements $g^{(2)}(0) < 0.14$ for all channels. The modularity of this distributed APIC–quantum memory system simplifies the quantum control problem, potentially enabling further scaling to thousands of channels.

https://doi.org/10.1364/OPTICA.486361

1. INTRODUCTION

Solid-state artificial atoms [1], many of which have long-lived quantum memories [2–5], can achieve photon-mediated remote entanglement [6,7], and can be heterogeneously integrated with photonics [8,9], are a promising platform for the construction of large-scale quantum networks [10–12]. The networking of these atom-like emitters requires an efficient and high-fidelity optical interface for both reconfigurable optical addressing and collection of photoluminescence (PL) at visible wavelengths. The optical control layer thus presents two challenges: i) scalable high-fidelity manipulation of optical fields at high speeds, which necessitates high-quality optical switches in atom-control photonic integrated circuit (APIC) [13] platforms; and ii) scalable high-efficiency photon collection from remotely addressable single emitters. While previously demonstrated visible-wavelength APIC platforms such as thin-film lithium niobate [14–16], thermally tuned silicon nitride [17–20], and piezoelectrically actuated silicon nitride [21–24] all have promise for scalability (for example, up to 16 channels [14,20]), none currently combine optically broadband operation, high switching contrast (>40 dB) at nanosecond timescales, and low-voltage operation. Other multi-channel optical control systems have been applied to trapped ion systems

[25,26] and large arrays of neutral atoms [27], but used only passive PICs or bulk components without independent pulse control. On the photon collection side, efficient collection has been demonstrated using standard confocal microscopy [28–30], by leveraging photonic nanostructures such as immersion lenses [31–33] and cavities [8,34–37], or single-channel fiber collection from tapered waveguides [8,38,39]. Collection through a heterogeneously integrated photonic chip [9,40,41] at the cost of some optical loss due to the diamond–chip interface has also been reported. To date, these past works treated each side of the optical control layer separately, but there remains an open question of how to combine the requirements of i) and ii) into a single scalable system.

Here we introduce an architecture for the optical control layer consisting of modular piezoelectrically actuated APICs and diamond microchiplets with implanted single emitters. In this configuration, the excitation and collection optical paths are perpendicular, enabling the inverse tapered diamond waveguides to take advantage of free-space modal conversion for efficient collection through the optical path parallel to the waveguides while maintaining the ability to selectively address a large area of distinct emitters through the perpendicular path. We demonstrate our control scheme by first satisfying requirement i) through our APIC switch, implemented as a four-channel binary tree mesh [13] with visible-wavelength switching and power routing capabilities. The APIC's switching circuit uses a triple-phase shifter design that takes advantage of hardware error correction [42,43] and a stronger strain-optic response than previous designs, enabling low switching voltages while maintaining high-contrast (>40 dB) and high-speed (>30 MHz) switching performance. The switch's architecture is nonresonant and optically broadband, with the phase shifters having demonstrated high extinction between 705 and 780 nm [23]. Moreover, the large transparency window of SiN enables the switch to function at shorter wavelengths down to 500 nm with optimized waveguide and phase-shifter dimensions. The switch shows negligible crosstalk between channels and enables repeatable arbitrary pulse carving on all four outputs, combined with >1 MHz power balancing between ports. We further demonstrate requirement ii) by applying the APIC to a local group of quantum emitters by projecting the optical output channels onto ion-implanted silicon vacancy color centers (SiVs) [32,44] in diamond microchiplets [9] mounted in a 5 K cryostat. Through PL excitation (PLE) and second-order autocorrelation measurements, we demonstrate optical addressing with independent temporal control of four spatially distinct color centers and achieve high (∼15%) collection efficiency, single emitter linewidths of 152 MHz–287 MHz, and $g^{(2)}(0)$ of 0.06–0.14. The modularity of this architecture allows for easy switching between different sets of quantum emitters by adding different sets of diamond microchiplets into the cryostat setup. Our APIC excitation and diamond collection techniques should enable scalable quantum control of emitters as part of a larger network of quantum nodes.

2. PHOTONIC INTEGRATED SWITCH DESIGN AND OPERATION

The schematic of our APIC-to-diamond control architecture is as follows. The APIC design consists of a "single" routing Mach–Zehnder Interferometer (MZI) [Fig. 1(a)] and a "triple" switching MZI [Fig. 1(b)] arranged in a binary tree architecture [Fig. 1(c)]. A single cantilever phase shifter (CPS) [23] in the routing MZIs directs the desired amount of light to the appropriate outputs. The switching MZI uses three phase shifters: two CPSs that enable optically broadband and high-fidelity routing (>40 dB) for cross and bar ports using hardware error correction robust to fabrication imperfections [43] and a third, strain-optic phase shifter (SPS)

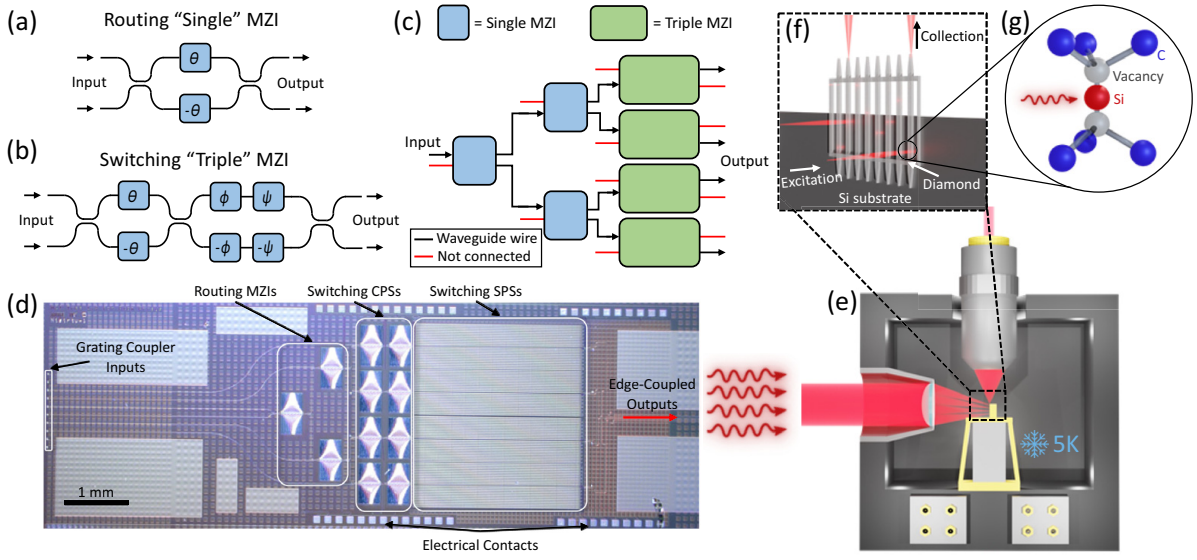

Fig. 1. Photonic integrated network switch architecture for local addressing of multiple quantum emitters. (a) Routing "single" MZIs to split the single input into each of the four ports and (b) switching "triple" MZIs that enable fast arbitrary pulsing of light with high extinction. The routing MZIs consist of a single cantilever phase shifter (CPS) and two 50:50 directional couplers, while the switching MZIs consist of two CPSs, a strain-optic phase shifter (SPS), and three 50:50 couplers. (c) Schematic of the binary tree switch design. (d) Microscope image of the fabricated integrated network switch with the CPSs and SPSs labeled. Light is input through grating couplers on the left side and collected through edge-coupled outputs on the right. The APIC is fabricated with 400 nm × 300 nm rectangular SiN waveguides and is actuated using piezoelectric AlN. (e) Cryostat setup housing the quantum emitters with light from the switch projected through free space for quantum control experiments. (f) Diamond quantum microchiplet overhanging a Si substrate with (g) implanted Si vacancy color centers with light pulses from the chip controlling the optical emission. The diamond nanostructure allows for high-efficiency collection of the emitter's emission.

[22,45], that enables a fast phase response for on–off switching of the output channel. The MZI's bar output port is defined as the output on the same side as the input light port, and the cross output port is the output on the opposite side of the input light port. During operation, a CPU controller programs the two CPSs to route the light to a dump port while the SPS is held at 0 V. We then can send an arbitrary pulse sequence to the SPS to switch the light to the output port without having to change the applied DC voltages to the CPSs.

A microscope image of the APIC is shown in Fig. 1(d), with the different phase shifters and electrical contacts labeled. We input light into the chip with an optical fiber array through a single grating leading to the routing MZIs, while other inputs are only used for device calibration. We then collect the edge-coupled light from each output with a high-NA objective, enabling imaging of the outputs into any system for optical control experiments. Figure 1(e) shows the optical imaging schematic where the output channels are projected into a cryostat to use for optical control of quantum emitters in diamond waveguides [Fig. 1(f)], such as SiVs [Fig. 1(g)]. The inverse-tapered diamond waveguides are in the form of a quantum microchiplet [9], for ease of pick and place transfer to the Si chip. We chose overhanging waveguides for this architecture because this configuration enables perpendicular excitation and collection. The horizontal excitation normal to the diamond waveguides allows for scalable addressing of many color centers in the different waveguides of the array. The single photon fluorescence from the SiVs couples to the diamond waveguide mode, which then emits vertically into free space through the inverse tapered couplers, as shown in Fig. 1(f). This free-space collection allows for efficient and scalable detection due to low-loss collection optics that are robust to misalignment when compared with fiber coupling or PIC integration. Electrical control of the integrated optical components is made through a custom printed circuit board (PCB) with wire bonds to the APIC. Commercial arbitrary waveform generator boards, embedded in a National Instruments PXIe system, control the CPSs and SPSs. A single board with 22 active channels controls the CPSs, providing ±25 V, and two boards with four channels of arbitrary waveform generation each control the SPSs, providing ±2.5 V. High-speed amplifiers on the PCB amplify the signals to the SPSs to ±12.5 V. The APIC is fabricated on 200 mm Si technology with a CMOS-compatible fabrication procedure, as detailed in prior works [22,23]. See Supplement 1, Sections 1 and 2 for more details on the optical and electrical components of the system.

Figure 2 summarizes the APIC characterization and calibration by monitoring the transmission of each edge-coupled optical output. For all optical tests, we use 737 nm wavelength laser light coupled into the TM mode of the on-chip 400 nm wide by 300 nm thick silicon nitride waveguides [modal shape simulated in Fig. 2(a)], which adiabatically expand to 5 μm wide in the SPS [Fig. 2(b)] to increase strain-optic sensitivity [22,45]. The less-confined TM mode takes advantage of a higher photoelastic responsivity when compared to the TE mode [46], resulting in a lower V_π of the phase shifter than previously reported [22]. Our DC calibration results for the routing MZIs [Fig. 2(c)] are shown in Figs. 2(d)–2(e) and for the switching MZIs [Fig. 2(f)] are shown in Figs. 2(g)–2(j), highlighting the low-voltage operation of the SPS for switching and high on–off extinction ratios. These high extinction ratios for the triple-phase shifter are enabled by the second CPS accounting for fabrication imperfections in the 50:50 directional couplers. The extinction values are repeatable over the course of multiple days of experiments with fine-tuned recalibration only necessary once a week or less. We do not notice any drift in the extinction voltages due to device heating over the course of our experiments. For calibration data for each of the output ports, see Supplement 1, Section 3.

3. PULSE CHARACTERIZATION AND STABILITY

We tested the optical pulse carving of our switch by applying representative pulse sequences to each of the SPSs in the switching MZIs. The "off" state of the output is defined to be 0 V due to the calibration procedure, and the full "on" state is achieved by applying the experimentally determined cross-state voltage. Pulses of varying amplitudes below the maximum are created by setting the applied voltage between these cross and bar states. Using time-resolved measurements on a 125 MHz photodiode, we found rise and fall times of ∼20 ns when programming a 200 ns pulse

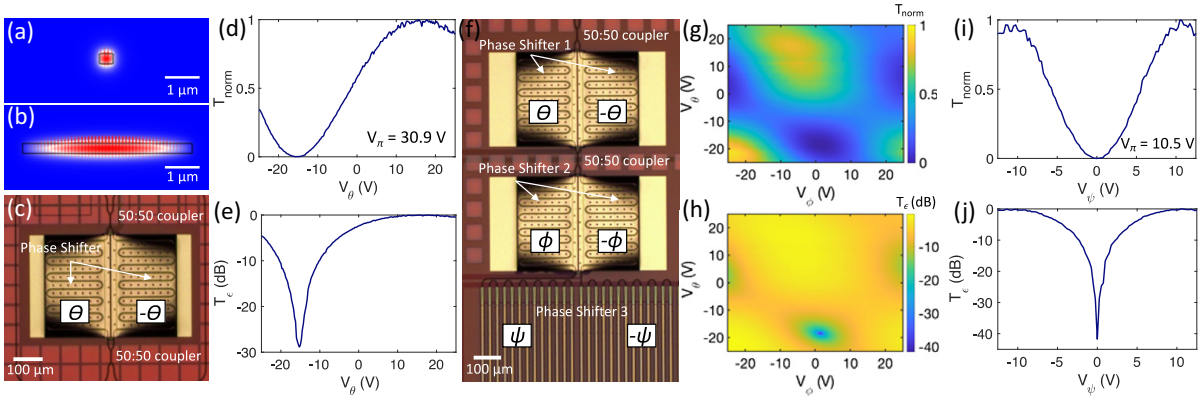

Fig. 2. Device performance and calibration. Simulated TM optical waveguide mode for (a) 400 nm waveguides and (b) 5 μm waveguides in the SPSs. (c) Microscope image of a routing MZI. A voltage is antisymmetrically applied to each side of the phase shifter to give the maximum actuation range. (d) Normalized transmission ($T_{\text{norm}} = T/T_{\max}$) and (e) extinction [$T_\epsilon = 10 * \log(T_{\text{norm}})$] measured from a single output with the applied voltage to the cantilever swept from −25 to 25 V. A single phase shifter achieves 25–30 dB extinction. (f) Microscope image of a switching MZI with three phase shifters. The first two CPSs are calibrated with the SPS held at 0 V to maximize output port extinction. (g) Normalized transmission T_{norm} and (h) extinction T_ϵ plots measured from sweeping the applied voltages of the two CPSs. The addition of the second cantilever compared to the single MZI allows for the output extinction to exceed 40 dB. (i) Normalized transmission T_{norm} and (j) extinction T_ϵ plots for the SPS, calibrated after the two CPSs in the switching MZI.

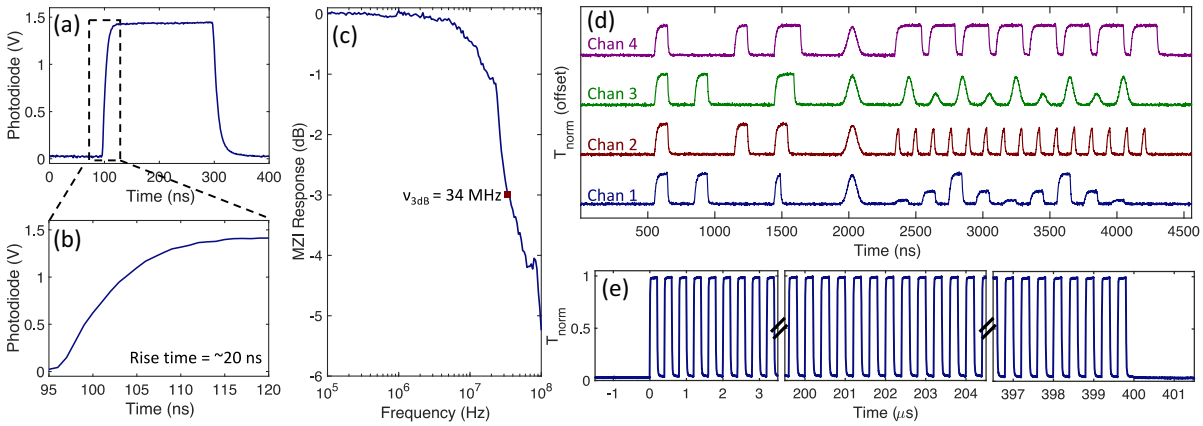

Fig. 3. High-speed device pulsing qualification. (a) Measured 200 ns pulse from an output port of the chip and (b) inset of the pulse showing a ∼20 ns rise time from the SPS. (c) Normalized modulator response for a 3 V sinusoidal signal showing the −3 dB cutoff at $\nu_{3\,\mathrm{dB}} = 34$ MHz. (d) Pulsing scheme showing the capabilities of the binary tree for arbitrary pulsing schemes. Each output can be pulsed at arbitrary times, lengths, shapes, and amplitudes. (e) Repeated 200 ns pulses with a 50% duty cycle to measure the consistency of our device. The standard deviation of the integrated pulse area is 6.8×10^{-4} for 1000 consecutive pulses.

[Figs. 3(a) and 3(b)] for all channels. The small-signal frequency-resolved modular response [Fig. 3(c)] indicates a −3 dB cutoff at $\nu_{3\,\mathrm{dB}} = 34$ MHz, allowing for >30 MHz optical control of each channel. The device can also be run at higher modulation speeds (>100 MHz) with a trade-off of lower responsivity (< −6 dB). The speed of the SPS in this work is slightly reduced from previous demonstrations [22] due to a larger electrical series resistance and capacitance from the longer phase shifters, which may be alleviated with wider electrical routing wires.

To explore the optical control programmability, we tested various pulse sequences. Figure 3(d) shows the resulting measurement of each of the outputs and shows four different capabilities of this system: i) any set of outputs can be pulsed simultaneously, ii) each pulsewidth can be independently manipulated, iii) the waveform can be temporally amplitude modulated into different shapes, such as square or Gaussian, and iv) the pulse height can be independently set. With these criteria met, our chip has the ability to create a full set of quantum rotations [47]. Furthermore, we measured the consistency of the pulsing of our device by applying repeated 200 ns pulses with 200 ns intervals and measuring the deviations in each pulse. We find a pulse area consistency (1σ standard deviation) of 6.8×10^{-4} for 1000 pulses, showing robust pulse uniformity. Examples of these pulses from the beginning, middle, and end of this pulse sequence are shown in Fig. 3(e). Lastly, we did not observe crosstalk from thermal, electrical, or piezo effects between the different phase shifters (details in Supplement 1, Section 4).

4. INDEPENDENT ADDRESSING OF MULTIPLE SINGLE SiVs

To demonstrate the applicability of the APIC, we used it to resonantly drive individual emitters within an ensemble of SiVs. As shown in Fig. 4(a), the APIC projects each port perpendicularly onto separate diamond waveguides in a cryostat. The diamond waveguides are fabricated with inverse tapered end couplers oriented towards the collection path, allowing for a high collection efficiency of ∼15%. To calculate our collection efficiency, we assumed a quantum efficiency of 5% for our SiVs, which has been reported in the literature for diamond nanostructures [30,34]. Different nanostructuring techniques have yielded different calculated values for SiV quantum efficiency (e.g., 10% in [8]), adding some uncertainty to this assumption. See Supplement 1, Sections 5 and 6 for full diamond fabrication information and collection efficiency calculation. The inverse tapers confine the emitted PL to an NA much smaller than that of the collection optics, allowing for scalable collection. In the excitation path, we include a spatial light modulator (SLM) for small spatial adjustments to each projected beam. This allows us to independently steer each excitation spot to specific SiVs in the diamond waveguides. We note that once the SLM is initially programmed, it is kept static over the course of the experiment, making its slow reconfiguration time (∼100 Hz) inconsequential for the excitation experiments. We resonantly excite each of the SiVs while collecting the phonon sideband (PSB) emission using a 750 nm long pass filter to remove excess pump light. We projected this fluorescence onto an electron-multiplying charge-coupled device (EMCCD). Figure 4(b) shows acquisitions of 30 s of the collected fluorescence normalized to the brightest point of each image, with no further image processing. This sequence shows independent and simultaneous optical control of SiVs in four different diamond waveguides. Due to variations in the local strain throughout the diamond, the zero-phonon lines (ZPLs) have an inhomogeneous distribution that exceeds the excitation laser linewidth. Improved diamond fabrication procedures that introduce the Si during chemical vapor deposition have been shown to limit this inhomogeneity [48,49]. To collect SiV emission from multiple waveguides simultaneously, we increased the temperature of the diamond samples to broaden the ZPL linewidths so that they are spectrally overlapping. Thus, for these images, we likely addressed multiple emitters in each diamond waveguide due to the high density of SiVs in our sample (>50 emitters per waveguide).

However, to show the applicability of this scheme for controlling individual single emitters, we cooled the diamond sample to a base temperature of 5 K and repeated the excitation scheme with each channel projected onto a spectrally resolved SiV. Figures 5(a)–5(d) show the PLE frequency scans for SiVs in four different waveguides, demonstrating linewidths < 290 MHz. Second-order correlation measurements indicate strong antibunching, with a normalized $g^{(2)}(0)$ ranging from 0.06 ± 0.09 to 0.14 ± 0.11, well

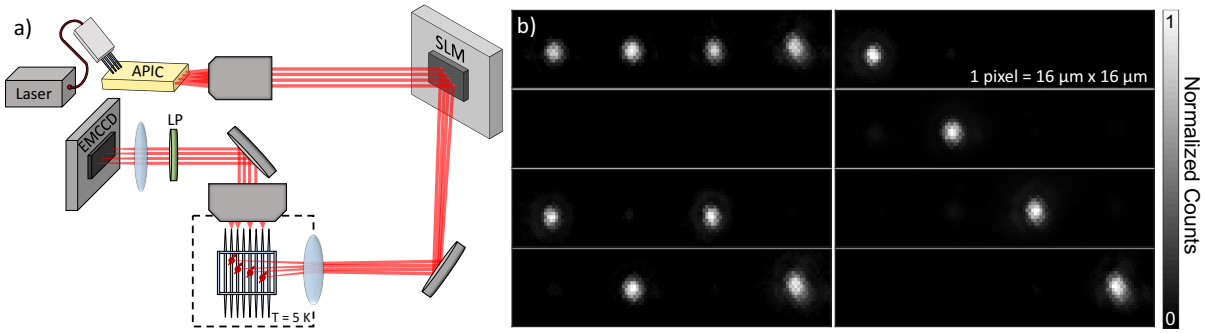

Fig. 4. Independent optical control of Si vacancy color centers. (a) Experimental setup. 737 nm laser light is input into the APIC through grating couplers. The four outputs are imaged onto a diamond microchiplet with the use of an SLM to steer the beams onto individual SiVs. The emission of the SiVs is collected, and the PSB is filtered out with a 750 nm long pass filter (LP), and imaged onto an EMCCD. (b) Simultaneous PLE measurements on four different diamond waveguides. By driving the APIC, emission from emitters in each waveguide can be independently controlled with high extinction. Each panel shows a different iteration of outputs being driven, showing complete independence of emitter emission.

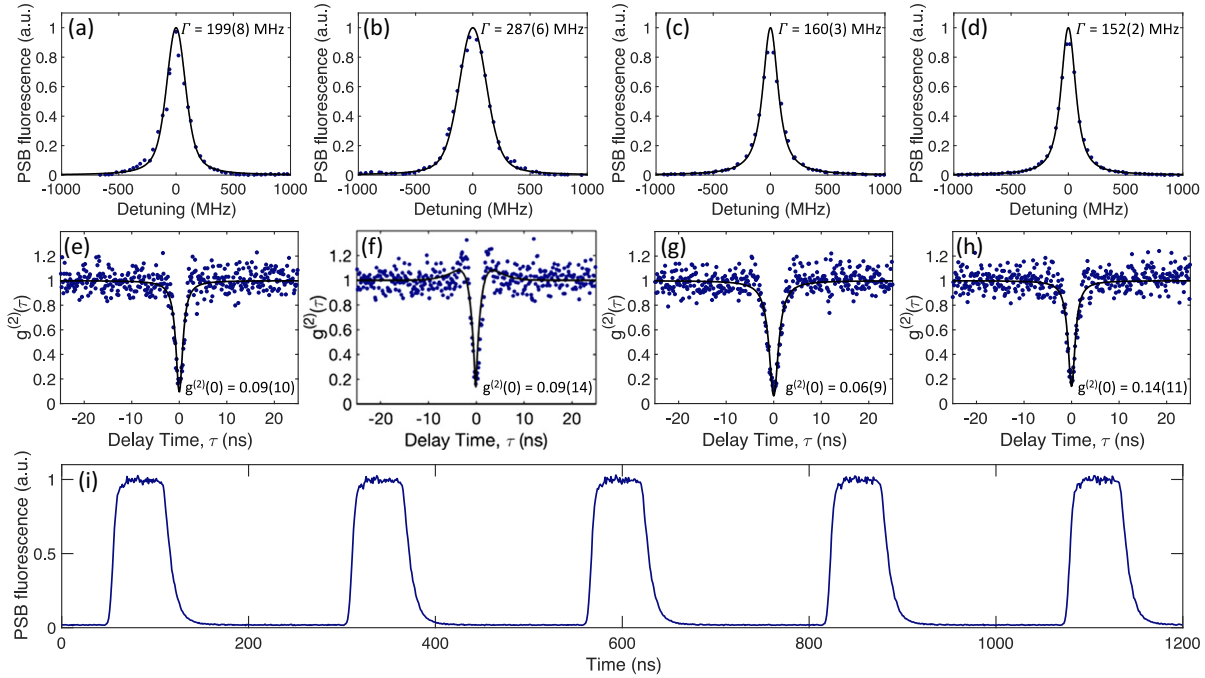

Fig. 5. Direct addressing and temporal control of single SiV emitters. (a)–(d) PLE spectrum of single SiVs excited with the APIC. Each vacancy is excited with light from a different APIC channel. (e)–(h) Autocorrelation measurements of the same single SiVs. For each emitter, $g^{(2)}(0) < 0.14$, well below the 0.5 threshold to demonstrate single photon emission. (i) Pulsed fluorescence demonstrating temporal control of the emission of a single emitter. Data shown is integrated over 3 min.

below the 0.5 threshold for single photon emission [Figs. 5(e)–5(h)]. We find an average emitter lifetime of 1.76(1) ns (see Supplement 1, Section 6), consistent with other measurements of ion-implanted SiVs [50]. With the outputs of the MZI tree projected on these emitters simultaneously, we send pulse sequences to temporally control the SiV emission. An example pulse train is shown in Fig. 5(i), where we repeatedly pulse one of the channels [Channel 3, Figs. 5(c) and 5(g)] with 100 ns pulses and a period of 250 ns and collect the fluorescence on a time-resolved avalanche photodiode, demonstrating temporal control of a single photon source. See Supplement 1, Section 7 for more details on the SiV linewidth and autocorrelation measurements.

5. DISCUSSION

We introduced and demonstrated a scalable optical control system for individual addressing of quantum atom-like emitters. We demonstrated that these emitters have single photon emission with spectral linewidths close to the lifetime limit of 93 MHz for SiVs, a necessary quality required for quantum networking. We achieved a high collection efficiency of 15%, which could be further improved by adding a Bragg reflector to the back half of our diamond waveguide, potentially increasing our collection efficiency by a factor of two. The modularity of the APICs and diamond microchiplets is scalable to thousands of ports and can be integrated with CMOS control electronics for VSLI devices. Operating voltages can be further reduced by allowing for a tradeoff of extinction and applied voltage; i.e., if only 30 dB extinction is required then the SPS can be pulsed with < 2.5 V applied signal. The diamond collection

architecture is also readily scalable, with high-efficiency collection of many waveguides enabled by the modal conversion of the waveguides to a 0.26 NA (see Supplement 1, Section 8). With the collection optics used in this setup, this allows for the scaling to 2975 waveguides with 3 μm spacing between waveguides in a linear array without a loss of collection efficiency. The losses on the chip currently limit the scalability of the platform, with a total measured insertion loss of −19.2 dB. This loss is dominated by a low grating coupler efficiency of 10%, which can be improved with design and fabrication iterations (see Supplement 1, Section 9 for improved grating coupler results >40 %). SiN grating couplers have had efficiencies up to 59% reported [51], which would substantially decrease the insertion loss of our device. Other designs, such adiabatic coupling with tapered fibers, could offer further improvements with reported single mode fiber to waveguide coupling efficiencies of 97% [52]. For this chip, we measure an average insertion loss of ∼1.5 dB and ∼3 dB for the CPS and SPS, respectively. We are currently working on improvements to our fabrication procedure to further decrease these phase shifter loss values.

Future work will use this platform for running independent optical control schemes of quantum emitters. Using already demonstrated strain tuning [53,54] and integrated microwave-line spin control [40], we envision a second chip built from the same APIC platform that enables spectral matching of SiV emission and coherent control of the spin qubits, necessary functionalities for quantum computation. Optical filtering, such as cross-polarization or coherent nulling, and time-gated detection will allow for collection and interference of ZPL photons. Our APIC excitation platform is compatible with other alternative diamond structures beyond waveguides. Once the beams are collected in free space, the static commercial SLM can beam steer each of the outputs into an arbitrary orientation to focus on structures such as diamond nanopillars [55,56] or immersion lenses [31–33]. More broadly, the broadband [22,23] APIC technology can be applied to other optically trapped atomic systems [25–27,57–61] and will enable near-future experiments in the area of optical quantum control.

Funding. The MITRE Corporation (Quantum Moonshot Program); Basic Energy Sciences (DE-SC0012704); National Science Foundation (RAISE TAQS program); Center for Integrated Nanotechnologies.

Acknowledgment. M.D. and M.Z. thank MITRE engineers L. Chan, K. Dauphinais, and S. Vergados for their support in building mechanical and electronic components. K.P. and M.D. thank S. Trajtenberg and Y. S. Duan for additional experimental support and C. Li and Y. Hu for helpful conversations and comments. D.E. acknowledges partial support from Brookhaven National Laboratory, which is supported by the U.S. Department of Energy, Office of Basic Energy Sciences. M.E. performed this work, in part, with funding from the Center for Integrated Nanotechnologies, an Office of Science User Facility operated for the U.S. Department of Energy Office of Science.

Disclosures. D.E. is a scientific advisor to and holds shares in QuEra Computing.

Data availability. Data underlying the results presented in this paper are not publicly available at this time but may be obtained from the authors upon reasonable request.

Supplemental document. See Supplement 1 for supporting content.

REFERENCES

1. M. Atatüre, D. Englund, N. Vamivakas, S.-Y. Lee, and J. Wrachtrup, "Material platforms for spin-based photonic quantum technologies," Nat. Rev. Mater. **3**, 38–51 (2018).
2. N. Bar-Gill, L. M. Pham, A. Jarmola, D. Budker, and R. L. Walsworth, "Solid-state electronic spin coherence time approaching one second," Nat. Commun. **4**, 1743 (2013).
3. C. E. Bradley, J. Randall, M. H. Abobeih, R. C. Berrevoets, M. J. Degen, M. A. Bakker, M. Markham, D. J. Twitchen, and T. H. Taminiau, "A ten-qubit solid-state spin register with quantum memory up to one minute," Phys. Rev. X **9**, 031045 (2019).
4. M. V. G. Dutt, L. Childress, L. Jiang, E. Togan, J. Maze, F. Jelezko, A. S. Zibrov, P. R. Hemmer, and M. D. Lukin, "Quantum register based on individual electronic and nuclear spin qubits in diamond," Science **316**, 1312–1316 (2007).
5. P.-J. Stas, Y. Q. Huan, B. Machielse, E. N. Knall, A. Suleymanzade, B. Pingault, M. Sutula, S. W. Ding, C. M. Knaut, D. R. Assumpcao, Y.-C. Wei, M. K. Bhaskar, R. Riedinger, D. D. Sukachev, H. Park, M. Lončar, D. S. Levonian, and M. D. Lukin, "Robust multi-qubit quantum network node with integrated error detection," Science **378**, 557–560 (2022).
6. P. C. Humphreys, N. Kalb, J. P. J. Morits, R. N. Schouten, R. F. L. Vermeulen, D. J. Twitchen, M. Markham, and R. Hanson, "Deterministic delivery of remote entanglement on a quantum network," Nature **558**, 268–273 (2018).
7. B. Hensen, H. Bernien, A. E. Dréau, A. Reiserer, N. Kalb, M. S. Blok, J. Ruitenberg, R. F. L. Vermeulen, R. N. Schouten, C. Abellán, W. Amaya, V. Pruneri, M. W. Mitchell, M. Markham, D. J. Twitchen, D. Elkouss, S. Wehner, T. H. Taminiau, and R. Hanson, "Loophole-free Bell inequality violation using electron spins separated by 1.3 kilometres," Nature **526**, 682–686 (2015).
8. A. Sipahigil, R. E. Evans, D. D. Sukachev, M. J. Burek, J. Borregaard, M. K. Bhaskar, C. T. Nguyen, J. L. Pacheco, H. A. Atikian, C. Meuwly, R. M. Camacho, F. Jelezko, E. Bielejec, H. Park, M. Lončar, and M. D. Lukin, "An integrated diamond nanophotonics platform for quantum-optical networks," Science **354**, 847–850 (2016).
9. N. H. Wan, T.-J. Lu, K. C. Chen, M. P. Walsh, M. E. Trusheim, L. De Santis, E. A. Bersin, I. B. Harris, S. L. Mouradian, I. R. Christen, E. S. Bielejec, and D. Englund, "Large-scale integration of artificial atoms in hybrid photonic circuits," Nature **583**, 226–231 (2020).
10. M. A. Nielsen and I. L. Chuang, *Quantum Computation and Quantum Information*, 10th anniversary ed. (Cambridge University, 2010).
11. S. Wehner, D. Elkouss, and R. Hanson, "Quantum internet: a vision for the road ahead," Science **362**, eaam9288 (2018).
12. H. J. Kimble, "The quantum internet," Nature **453**, 1023–1030 (2008).
13. W. Bogaerts, D. Pérez, J. Capmany, D. A. B. Miller, J. Poon, D. Englund, F. Morichetti, and A. Melloni, "Programmable photonic circuits," Nature **586**, 207–216 (2020).
14. I. Christen, M. Sutula, T. Propson, H. Sattari, G. Choong, C. Panuski, A. Melville, J. Mallek, S. Hamilton, P. Benjamin Dixon, A. J. Menssen, D. Braje, A. H. Ghadimi, and D. Englund, "An integrated photonic engine for programmable atomic control," arXiv, arXiv:2208.06732 [quant-ph] (2022).
15. B. Desiatov, A. Shams-Ansari, M. Zhang, C. Wang, and M. Lončar, "Ultra-low-loss integrated visible photonics using thin-film lithium niobate," Optica **6**, 380–384 (2019).
16. C. Li, B. Chen, Z. Ruan, H. Wu, Y. Zhou, J. Liu, P. Chen, K. Chen, C. Guo, and L. Liu, "High modulation efficiency and large bandwidth thin-film lithium niobate modulator for visible light," Opt. Express **30**, 36394–36402 (2022).
17. G. Liang, H. Huang, A. Mohanty, M. C. Shin, X. Ji, M. J. Carter, S. Shrestha, M. Lipson, and N. Yu, "Robust, efficient, micrometre-scale phase modulators at visible wavelengths," Nat. Photonics **15**, 908–913 (2021).
18. A. Mohanty, Q. Li, M. A. Tadayon, S. P. Roberts, G. R. Bhatt, E. Shim, X. Ji, J. Cardenas, S. A. Miller, A. Kepecs, and M. Lipson, "Reconfigurable nanophotonic silicon probes for sub-millisecond deep-brain optical stimulation," Nat. Biomed. Eng. **4**, 223–231 (2020).
19. Z. Yong, H. Chen, X. Luo, A. Govdeli, H. Chua, S. S. Azadeh, A. Stalmashonak, G.-Q. Lo, J. K. S. Poon, and W. D. Sacher, "Power-efficient silicon nitride thermo-optic phase shifters for visible light," Opt. Express **30**, 7225–7237 (2022).
20. C. Taballione, T. A. W. Wolterink, J. Lugani, A. Eckstein, B. A. Bell, R. Grootjans, I. Visscher, D. Geskus, C. G. H. Roeloffzen, J. J. Renema,

I. A. Walmsley, P. W. H. Pinkse, and K.-J. Boller, "8 × 8 reconfigurable quantum photonic processor based on silicon nitride waveguides," Opt. Express **27**, 26842–26857 (2019).
21. A. J. Menssen, A. Hermans, I. Christen, T. Propson, C. Li, A. J. Leenheer, M. Zimmermann, M. Dong, H. Larocque, H. Raniwala, G. Gilbert, M. Eichenfield, and D. R. Englund, "Scalable photonic integrated circuits for programmable control of atomic systems," arXiv, arXiv:2210.03100 [physics.optics] (2022).
22. M. Dong, G. Clark, A. J. Leenheer, M. Zimmermann, D. Dominguez, A. J. Menssen, D. Heim, G. Gilbert, D. Englund, and M. Eichenfield, "High-speed programmable photonic circuits in a cryogenically compatible, visible–near-infrared 200 mm CMOS architecture," Nat. Photonics **16**, 59–65 (2021).
23. M. Dong, D. Heim, A. Witte, G. Clark, A. J. Leenheer, D. Dominguez, M. Zimmermann, Y. H. Wen, G. Gilbert, D. Englund, and M. Eichenfield, "Piezo-optomechanical cantilever modulators for VLSI visible photonics," APL Photon. **7**, 051304 (2022).
24. J. Wang, K. Liu, M. W. Harrington, R. Q. Rudy, and D. J. Blumenthal, "Silicon nitride stress-optic microresonator modulator for optical control applications," Opt. Express **30**, 31816–31827 (2022).
25. R. J. Niffenegger, J. Stuart, C. Sorace-Agaskar, D. Kharas, S. Bramhavar, C. D. Bruzewicz, W. Loh, R. T. Maxson, R. McConnell, D. Reens, G. N. West, J. M. Sage, and J. Chiaverini, "Integrated multi-wavelength control of an ion qubit," Nature **586**, 538–542 (2020).
26. K. K. Mehta, C. Zhang, M. Malinowski, T.-L. Nguyen, M. Stadler, and J. P. Home, "Integrated optical multi-ion quantum logic," Nature **586**, 533–537 (2020).
27. S. Ebadi, T. T. Wang, H. Levine, A. Keesling, G. Semeghini, A. Omran, D. Bluvstein, R. Samajdar, H. Pichler, W. W. Ho, S. Choi, S. Sachdev, M. Greiner, V. Vuletić, and M. D. Lukin, "Quantum phases of matter on a 256-atom programmable quantum simulator," Nature **595**, 227–232 (2021).
28. J. N. Becker, B. Pingault, D. Groß, M. Gündoğan, N. Kukharchyk, M. Markham, A. Edmonds, M. Atatüre, P. Bushev, and C. Becher, "All-optical control of the silicon-vacancy spin in diamond at millikelvin temperatures," Phys. Rev. Lett. **120**, 053603 (2018).
29. J. N. Becker, J. Görlitz, C. Arend, M. Markham, and C. Becher, "Ultrafast all-optical coherent control of single silicon vacancy colour centres in diamond," Nat. Commun. **7**, 13512 (2016).
30. E. Neu, M. Agio, and C. Becher, "Photophysics of single silicon vacancy centers in diamond: implications for single photon emission," Opt. Express **20**, 19956–19971 (2012).
31. L. Robledo, L. Childress, H. Bernien, B. Hensen, P. F. A. Alkemade, and R. Hanson, "High-fidelity projective read-out of a solid-state spin quantum register," Nature **477**, 574–578 (2011).
32. C. Hepp, T. Müller, V. Waselowski, J. N. Becker, B. Pingault, H. Sternschulte, D. Steinmüller-Nethl, A. Gali, J. R. Maze, M. Atatüre, and C. Becher, "Electronic structure of the silicon vacancy color center in diamond," Phys. Rev. Lett. **112**, 036405 (2014).
33. T. Schröder, F. Gädeke, M. J. Banholzer, and O. Benson, "Ultrabright and efficient single-photon generation based on nitrogen-vacancy centres in nanodiamonds on a solid immersion lens," New J. Phys. **13**, 055017 (2011).
34. J. Riedrich-Möller, C. Arend, C. Pauly, F. Mücklich, M. Fischer, S. Gsell, M. Schreck, and C. Becher, "Deterministic coupling of a single silicon-vacancy color center to a photonic crystal cavity in diamond," Nano Lett. **14**, 5281–5287 (2014).
35. J. Benedikter, H. Kaupp, T. Hümmer, Y. Liang, A. Bommer, C. Becher, A. Krueger, J. M. Smith, T. W. Hänsch, and D. Hunger, "Cavity-enhanced single-photon source based on the silicon-vacancy center in diamond," Phys. Rev. Appl. **7**, 024031 (2017).
36. J. C. Lee, I. Aharonovich, A. P. Magyar, F. Rol, and E. L. Hu, "Coupling of silicon-vacancy centers to a single crystal diamond cavity," Opt. Express **20**, 8891–8897 (2012).
37. J. L. Zhang, S. Sun, M. J. Burek, C. Dory, Y.-K. Tzeng, K. A. Fischer, Y. Kelaita, K. G. Lagoudakis, M. Radulaski, Z.-X. Shen, N. A. Melosh, S. Chu, M. Lončar, and J. Vučković, "Strongly cavity-enhanced spontaneous emission from silicon-vacancy centers in diamond," Nano Lett. **18**, 1360–1365 (2018).
38. J. A. Martínez, R. A. Parker, K. C. Chen, C. M. Purser, L. Li, C. P. Michaels, A. M. Stramma, R. Debroux, I. B. Harris, M. H. Appel, E. C. Nichols, M. E. Trusheim, D. A. Gangloff, D. Englund, and M. Atatüre, "Photonic indistinguishability of the tin-vacancy center in nanostructured diamond," Phys. Rev. Lett. **129**, 173603 (2022).
39. M. K. Bhaskar, D. D. Sukachev, A. Sipahigil, R. E. Evans, M. J. Burek, C. T. Nguyen, L. J. Rogers, P. Siyushev, M. H. Metsch, H. Park, F. Jelezko, M. Lončar, and M. D. Lukin, "Quantum nonlinear optics with a germanium-vacancy color center in a nanoscale diamond waveguide," Phys. Rev. Lett. **118**, 223603 (2017).
40. D. A. Golter, G. Clark, T. El Dandachi, S. Krastanov, A. J. Leenheer, N. H. Wan, H. Raniwala, M. Zimmermann, M. Dong, K. C. Chen, L. Li, M. Eichenfield, G. Gilbert, and D. Englund, "Multiplexed control of spin quantum memories in a photonic circuit," arXiv, arXiv:2209.11853 [quant-ph] (2022).
41. S. L. Mouradian, T. Schröder, C. B. Poitras, L. Li, J. Goldstein, E. H. Chen, M. Walsh, J. Cardenas, M. L. Markham, D. J. Twitchen, M. Lipson, and D. Englund, "Scalable integration of long-lived quantum memories into a photonic circuit," Phys. Rev. X **5**, 031009 (2015).
42. D. A. B. Miller, "Perfect optics with imperfect components," Optica **2**, 747–750 (2015).
43. M. Wang, A. Ribero, Y. Xing, and W. Bogaerts, "Tolerant, broadband tunable 2 × 2 coupler circuit," Opt. Express **28**, 5555–5566 (2020).
44. D. D. Sukachev, A. Sipahigil, C. T. Nguyen, M. K. Bhaskar, R. E. Evans, F. Jelezko, and M. D. Lukin, "Silicon-vacancy spin qubit in diamond: a quantum memory exceeding 10 ms with single-shot state readout," Phys. Rev. Lett. **119**, 223602 (2017).
45. P. R. Stanfield, A. J. Leenheer, C. P. Michael, R. Sims, and M. Eichenfield, "CMOS-compatible, piezo-optomechanically tunable photonics for visible wavelengths and cryogenic temperatures," Opt. Express **27**, 28588–28605 (2019).
46. F. Gyger, J. Liu, F. Yang, J. He, A. S. Raja, R. N. Wang, S. A. Bhave, T. J. Kippenberg, and L. Thévenaz, "Observation of stimulated Brillouin scattering in silicon nitride integrated waveguides," Phys. Rev. Lett. **124**, 013902 (2020).
47. J.-S. Li, J. Ruths, T.-Y. Yu, H. Arthanari, and G. Wagner, "Optimal pulse design in quantum control: a unified computational method," Proc. Natl. Acad. Sci. USA **108**, 1879–1884 (2011).
48. A. Sipahigil, K. D. Jahnke, L. J. Rogers, T. Teraji, J. Isoya, A. S. Zibrov, F. Jelezko, and M. D. Lukin, "Indistinguishable photons from separated silicon-vacancy centers in diamond," Phys. Rev. Lett. **113**, 113602 (2014).
49. L. J. Rogers, K. D. Jahnke, T. Teraji, L. Marseglia, C. Müller, B. Naydenov, H. Schauffert, C. Kranz, J. Isoya, L. P. McGuinness, and F. Jelezko, "Multiple intrinsically identical single-photon emitters in the solid state," Nat. Commun. **5**, 4739 (2014).
50. C. Wang, C. Kurtsiefer, H. Weinfurter, and B. Burchard, "Single photon emission from SiV centres in diamond produced by ion implantation," J. Phys. B **39**, 37 (2005).
51. S. Romero-García, F. Merget, F. Zhong, H. Finkelstein, and J. Witzens, "Visible wavelength silicon nitride focusing grating coupler with AlCu/TiN reflector," Opt. Lett. **38**, 2521–2523 (2013).
52. T. G. Tiecke, K. P. Nayak, J. D. Thompson, T. Peyronel, N. P. de Leon, V. Vuletić, and M. D. Lukin, "Efficient fiber-optical interface for nanophotonic devices," Optica **2**, 70–75 (2015).
53. S. Meesala, Y.-I. Sohn, B. Pingault, *et al.*, "Strain engineering of the silicon-vacancy center in diamond," Phys. Rev. B **97**, 205444 (2018).
54. G. Clark, M. Koppa, K. Chen, A. Leenheer, L. Li, D. Dominguez, M. Dong, M. Saha, D. A. Golter, G. Gilbert, M. Eichenfield, and D. Englund, "Piezoelectric control of spin quantum memories in a cryogenic programmable photonic circuit platform," in *Conference on Lasers and Electro-Optics (CLEO)* (2022), pp. 1–2.
55. R. Debroux, C. P. Michaels, C. M. Purser, N. Wan, M. E. Trusheim, J. Arjona Martínez, R. A. Parker, A. M. Stramma, K. C. Chen, L. de Santis, E. M. Alexeev, A. C. Ferrari, D. Englund, D. A. Gangloff, and M. Atatüre, "Quantum control of the tin-vacancy spin qubit in diamond," Phys. Rev. X **11**, 041041 (2021).
56. J. L. Zhang, K. G. Lagoudakis, Y.-K. Tzeng, C. Dory, M. Radulaski, Y. Kelaita, K. A. Fischer, S. Sun, Z.-X. Shen, N. A. Melosh, S. Chu, and J. Vučković, "Complete coherent control of silicon vacancies in diamond nanopillars containing single defect centers," Optica **4**, 1317–1321 (2017).
57. S. Debnath, N. M. Linke, C. Figgatt, K. A. Landsman, K. Wright, and C. Monroe, "Demonstration of a small programmable quantum computer with atomic qubits," Nature **536**, 63–66 (2016).
58. J. M. Pino, J. M. Dreiling, C. Figgatt, J. P. Gaebler, S. A. Moses, M. S. Allman, C. H. Baldwin, M. Foss-Feig, D. Hayes, K. Mayer, C. Ryan-Anderson, and B. Neyenhuis, "Demonstration of the trapped-ion quantum CCD computer architecture," Nature **592**, 209–213 (2021).

59. A. Lambrecht, J. Schmidt, P. Weckesser, M. Debatin, L. Karpa, and T. Schaetz, "Long lifetimes and effective isolation of ions in optical and electrostatic traps," Nat. Photonics **11**, 704–707 (2017).
60. H. Levine, A. Keesling, G. Semeghini, A. Omran, T. T. Wang, S. Ebadi, H. Bernien, M. Greiner, V. Vuletić, H. Pichler, and M. D. Lukin, "Parallel implementation of high-fidelity multiqubit gates with neutral atoms," Phys. Rev. Lett. **123**, 170503 (2019).
61. T. M. Graham, Y. Song, J. Scott, *et al.*, "Multi-qubit entanglement and algorithms on a neutral-atom quantum computer," Nature **604**, 457–462 (2022).